Hydrothermal Growth of Hierarchical Ni_3S_2 and Co_3S_4 on a Reduced Graphene Oxide Hydrogel@Ni Foam: A High-Energy-Density Aqueous Asymmetric Supercapacitor

Debasis Ghosh and Chapal Kumar Das*

Materials Science Centre, Indian Institute of Technology, Kharagpur, India

S Supporting Information

ABSTRACT: Ni foam@reduced graphene oxide (rGO) hydrogel−Ni_3S_2 and Ni foam@rGO hydrogel−Co_3S_4 composites have been successfully synthesized with the aid of a two-step hydrothermal protocol, where the rGO hydrogel is sandwiched between the metal sulfide and Ni foam substrate. Sonochemical deposition of exfoliated rGO on Ni foam with subsequent hydrothermal treatment results in the formation of a rGO-hydrogel-coated Ni foam. Then second-time hydrothermal treatment of the dried Ni@rGO substrate with corresponding metal nitrate and sodium sulfide results in individual uniform growth of porous Ni_3S_2 nanorods and a

Co_3S_4 self-assembled nanosheet on a Ni@rGO substrate. Both Ni@rGO−Ni_3S_2 and Ni@rGO−Co_3S_4 have been electrochemically characterized in a 6 M KOH electrolyte, exhibiting high specific capacitance values of 987.8 and 1369 F/g, respectively, at 1.5 A/g accompanied by the respective outstanding cycle stability of 97.9% and 96.6% at 12 A/g over 3000 charge−discharge cycles. An advanced aqueous asymmetric (AAS) supercapacitor has been fabricated by exploiting the as-prepared Ni@rGO−Co_3S_4 as a positive electrode and Ni@rGO−Ni_3S_2 as a negative electrode. The as-fabricated AAS has shown promising energy densities of 55.16 and 24.84 Wh/kg at high power densities of 975 and 13000 W/kg, respectively, along with an excellent cycle stability of 96.2% specific capacitance retention over 3000 charge−discharge cycles at 12 A/g. The enhanced specific capacitance, stupendous cycle stability, elevated energy density, and a power density as an AAS of these electrode materials indicate that it could be a potential candidate in the field of supercapacitors.

KEYWORDS: supercapacitor, energy density, power density, graphene, pseudocapacitance, specific capacitance
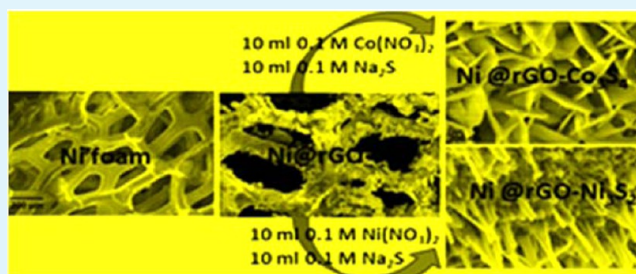
1. INTRODUCTION

Increasing awareness of the global effect and pollution caused by the atomic power source and depletion of fossil fuel has motivated exploration of alternative energy resources. Although solar cells, water turbines, or wind turbines may be considered promising alternatives, their intermittent nature still limits them as primary energy sources. Supercapacitors can be considered alternative energy storage systems with hybrid properties of batteries and capacitors in terms of both high energy density and high power density accompanied by high cycle life.[1] The charge-storage mechanism in a supercapacitor is solely dependent on its electrode material and supporting electrolyte. High-surface-area carbonaceous materials like carbon nanotube (CNT), graphene, and activated carbon having no redox-active functionality can act as electrical double-layer capacitors (EDLCs), and the charge stored is purely electrostatic in nature.[1] Redox-active transition-metal oxides or conducting polymers are established sources of pseudocapacitors and are capable of storing a larger amount of charge via electron-transfer faradaic reaction. Cobalt and nickel are the two most studied transition metals, the oxides[2,3]/hydroxides[4,5]/molybdates[6,7] of which have shown promising electrochemical

behavior because of the high redox activity of the metal ions. However, electrochemical investigation regarding the sulfide compounds of these two transition metals is still in the primary stage and requires much attention because of the higher electrical conductivity and mechanical and thermal stability compared to that of their corresponding metal oxides and overall rich redox chemistry.[8] Nickel sulfide and cobalt sulfide may exist in several phases and different morphologies and exhibit a variety of specific capacitances depending on the morphology. For example, NiS hollow spheres, NiS nanoflowers, NiS_2 nanocubes, Ni_3S_2 nanoflakes, CoS_2 octahedra, CoS nanowires, hollow CoS hexagonal nanosheets, Co_9S_8 nanotubes, CoS nanospheres, and flowerlike CoS have been reported, exhibiting high specific capacitance values of 927 F/g (4.08 A/g), 857.76 F/g (2 A/g), 695 F/g (1.25 A/g), 1293 F/g (5 mA/cm^2), 236.5 F/g (1 A/g), 508 F/g (2.5 mA/cm^2), 326.4 F/g (64.6 A/g), 285 F/g (0.5 A/g), 383 F/g (5 mV/s), 586 F/g (1 A/g), respectively.[9−18] Apart from the nickel and cobalt

sulfides, recently some other metal sulfides have also been investigated. Ramadoss et al. have reported nanostructured MoS_2, exhibiting a maximum specific capacitance of 403 F/g at 1 mV/s,[19] which was higher than that of 3D flowerlike MoS_2, exhibiting a maximum specific capacitance of 168 F/g at 1 A/g current in a 1 M KCl electrolyte.[20] Recently, Ratha and Rout have reported sheetlike WS_2 and its composite with reduced graphene oxide (rGO), showing specific capacitances of 70 and 350 F/g, respectively, at a 2 mV/s scan rate.[21]

Although the specific capacitance is good, the neat pseudocapacitive materials often suffer from swelling and shrinking during consecutive charging and discharging, resulting in a poor cycle life. A hybrid composite of these pseudocapacitive materials with high-surface-area carbon materials can be effective in this respect. Graphene is a 2D combination of an sp^2-hybridized carbon atom with the unique properties of high conductivity, high specific surface area, and the highest flexibility. A few approaches to prepare a hybrid composite of these pseudocapacitive metal sulfides with a high-surface-area double-layer capacitive material, like CNT, graphene, etc. It has been found that the hybrid material in the form of a composite of both the EDLC and pseudocapacitive materials exhibits superior electrochemical behavior in terms of both high cycle life and high specific capacitance.[21−26]

Still, the problem with the supercapacitor is its low working potential, which restricts its energy density. An attempt to fabricate an asymmetric electrode configuration of pseudocapacitive material with EDLC material or a hybrid composite material can be helpful in increasing the energy density where the pseudocapacitive material will lead the energy density due to high specific capacitance and the EDLC will lead the high power density.[27]

In our present study, we have prepared rGO-based hybrid composites of Ni_3S_2 and Co_3S_4 grown on Ni foam by a two-step hydrothermal approach, where the rGO hydrogel is sandwiched between the metal sulfide and Ni foam. The prepared Ni_3S_2 and Co_3S_4 showed pure phase and different architectures of nanorods and self-assembled cross-linked nanosheets, respectively. The as-prepared Ni@rGO−Ni_3S_2 and Ni@rGO−Co_3S_4 were electrochemically characterized as working electrodes in a 6 M KOH electrolyte to investigate their supercapacitive behavior. To understand the effect of rGO on the electrochemical performance of Ni_3S_2 and Co_3S_4, we also prepared Ni@Ni_3S_2 and Ni@Co_3S_4 electrodes without using rGO. In order to get a superior supercapacitive property, we have also fabricated an asymmetric supercapacitor, where the as-prepared Ni@rGO−Ni_3S_2 has been used as a negative electrode and the Ni@rGO−Co_3S_4 as a positive electrode.

2. RESULTS AND DISCUSSION

2.1. XRD Pattern. The XRD patterns of the as-prepared graphene oxide (GO) paper, rGO paper, and as-grown nickel and cobalt sulfide on Ni@rGO are shown in Figure 1. The XRD pattern of GO shows a sharp peak at $2\theta = 10.8°$ corresponding to the (001) plane. The successful flame reduction of the GO film is confirmed from the disappearance of the sharp (001) plane of the GO film and the appearance of a broad peak centered at $2\theta = 23.3°$, corresponding to the (002) plane of exfoliated graphene. The XRD patterns of the cobalt and nickel sulfide grown on Ni@rGO match well with respective JCPDS card nos. 01-071-4923 and 44-1418, indicating the formation of Co_3S_4 and Ni_3S_2. The crystalline
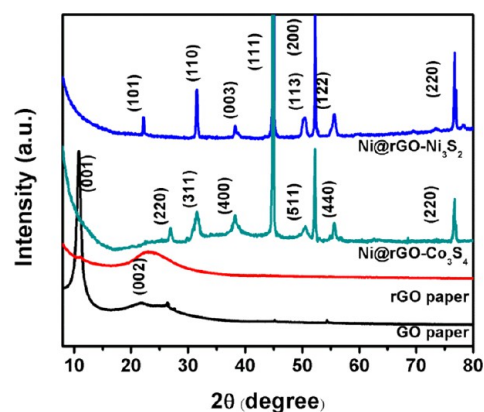

Figure 1. XRD patterns of the GO paper, rGO paper, Ni@rGO−Ni_3S_2, and Ni@rGO−Co_3S_4.

peaks at $2\theta = 44.8°$, 52.3°, and 76.8° correspond to the (111), (200), and (220) planes of Ni in the Ni foam.

2.2. Morphological Characterizations. The field-emission scanning electron microscopy (FESEM) images of the as-prepared GO paper surface and cross section are shown in parts a and b of Figure 2, respectively. The cross section indicates
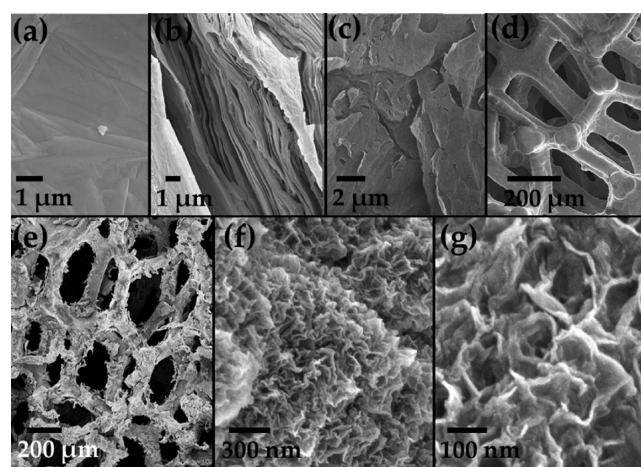

Figure 2. FESEM images of the as-prepared GO paper: (a) surface; (b) cross section. FESEM images of the surface of rGO paper after flame reduction (c), Ni foam (d), and the rGO hydrogel deposited on Ni foam after hydrothermal treatment (e). High-magnification image of the rGO hydrogel (f and g).

many GO layers. The smooth surface of the GO paper becomes rough in the flame-reduced rGO paper (Figure (2c) accompanied by about 10 times expansion, suggesting that the rGO sheets are well exfoliated. Parts d and e of Figure 2 represent the FESEM image of neat Ni foam and the rGO hydrogel uniformly coated Ni foam, respectively. The sonochemical deposition post hydrothermal treatment results in the formation of rGO hydrogel from the exfoliated rGO on the Ni foam. Parts f and g of Figure 2 represent the FESEM images of the as-formed rGO hydrogel at various magnifications, revealing its porous architecture.

The FESEM images of Ni@Ni_3S_2 and Ni@Co_3S_4 at different magnifications are shown in Figure S2 in the Supporting Information (SI). The FESEM images of the as-grown Ni_3S_2 and Co_3S_4 on Ni@rGO are shown in parts a−d and e−h of Figure 3, respectively, at various magnifications. The FESEM

images of Ni@rGO–Ni$_3$S$_2$ reveal the vertically aligned nanorod morphology of the as-grown Ni$_3$S$_2$ on a Ni@rGO substrate.
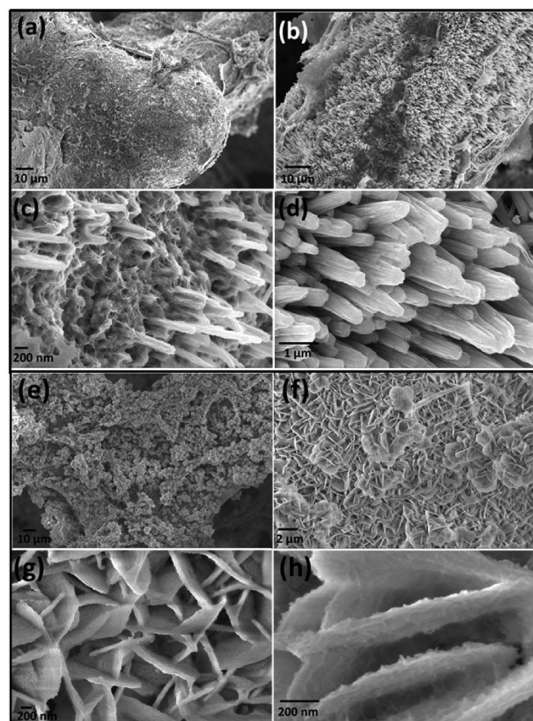

Figure 3. FESEM images of Ni@rGO–Ni$_3$S$_2$ at various magnifications (a and b) and growth of 1D Ni$_3$S$_2$ on the rGO hydrogel (c). High-magnification image of Ni$_3$S$_2$ nanorods (d). FESEM images of Ni@rGO–Co$_3$S$_4$ at various magnifications (e and f). Higher-magnification image of a cross-linked interconnected nanosheet of Co$_3$S$_4$ (g and h).

A nucleation center is created on the rGO hydrogel for the growth of Ni$_3$S$_2$ nanoparticles on the rGO surface, which then creates heterogeneous nucleation sites for further growth of Ni$_3$S$_2$ laterally, resulting in the formation of a 1D structure with average lengths of 1−3 μm and diameters of 100−300 nm. The nanorods are firmly bonded to the rGO hydrogel, as shown in Figure 3c. The FESEM images of Ni@rGO–Co$_3$S$_4$ indicate that Co$_3$S$_4$ is comprised of numerous ordered interconnected nanosheets, forming a mesoporous structure. The nanosheets are densely packed on the Ni@rGO substrate with an average sheet thickness in the range of 50−80 nm. The elemental mapping of Ni@rGO–Ni$_3$S$_2$ and Ni@rGO–Co$_3$S$_4$ is shown in Figures S3 and S4 in the SI, respectively. The elemental mapping also clearly indicates the distribution of Ni$_3$S$_2$ and Co$_3$S$_4$ over the rGO hydrogel.

Transmission electron microscopy (TEM) and high-resolution TEM (HRTEM) analyses of the as-prepared composites were carried out after scratching rGO–Ni$_3$S$_2$ and rGO–Co$_3$S$_4$ from the Ni foam. The TEM image of rGO–Ni$_3$S$_2$ (Figure 4a,b) also supports FESEM analysis of the 1D nanorod morphology of Ni$_3$S$_2$, one end of which is covered by the rGO hydrogel. The presence of both spot and ring patterns in the selected-area electron diffraction (SAED) pattern (Figure 4c) of rGO–Ni$_3$S$_2$ also confirms that the growth of Ni$_3$S$_2$ nanorods occurs from the rGO hydrogel. The HRTEM image of rGO–Co$_3$S$_4$ (Figure 4d) indicates that Co$_3$S$_4$ is composed of the crumpled nanosheets with many folded edges and is well distributed over the rGO surface. A highly magnified image of Co$_3$S$_4$ (Figure 4e) indicates a clear color contrast between the center and edge of the nanosheet network, signifying that a nucleation center is created on the rGO surface for the growth of Co$_3$S$_4$, which then creates a heterogeneous nucleation center for growth of the interconnected ordered mesoporous nanosheet network. In the SAED pattern on the Co$_3$S$_4$ sheet, both the ring and spot patterns coexist, indicating that the
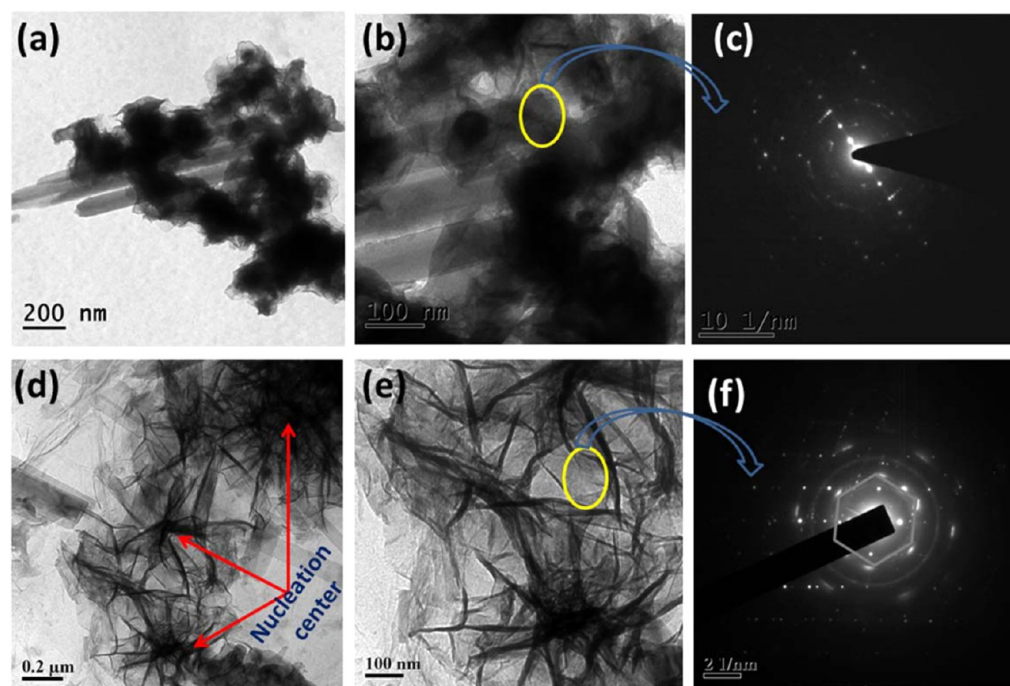

Figure 4. TEM image of rGO–Ni$_3$S$_2$ after scratching from Ni foam at various magnifications (a and b). SAED pattern on rGO–Ni$_3$S$_2$ (c). HRTEM image of rGO–Co$_3$S$_4$ after scratching from Ni foam at various magnifications (d and e). SAED pattern on rGO–Co$_3$S$_4$ (f).
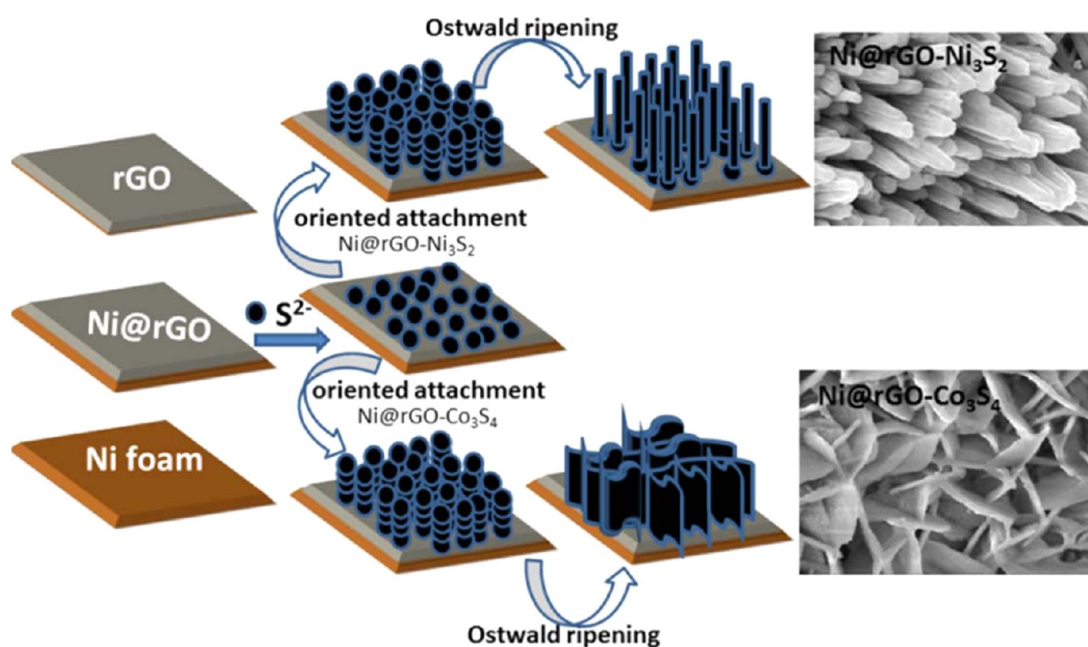
Figure 5. Schematic diagram of the growth of a Ni_3S_2 nanorod and a Co_3S_4 nanosheet network over Ni@rGO.
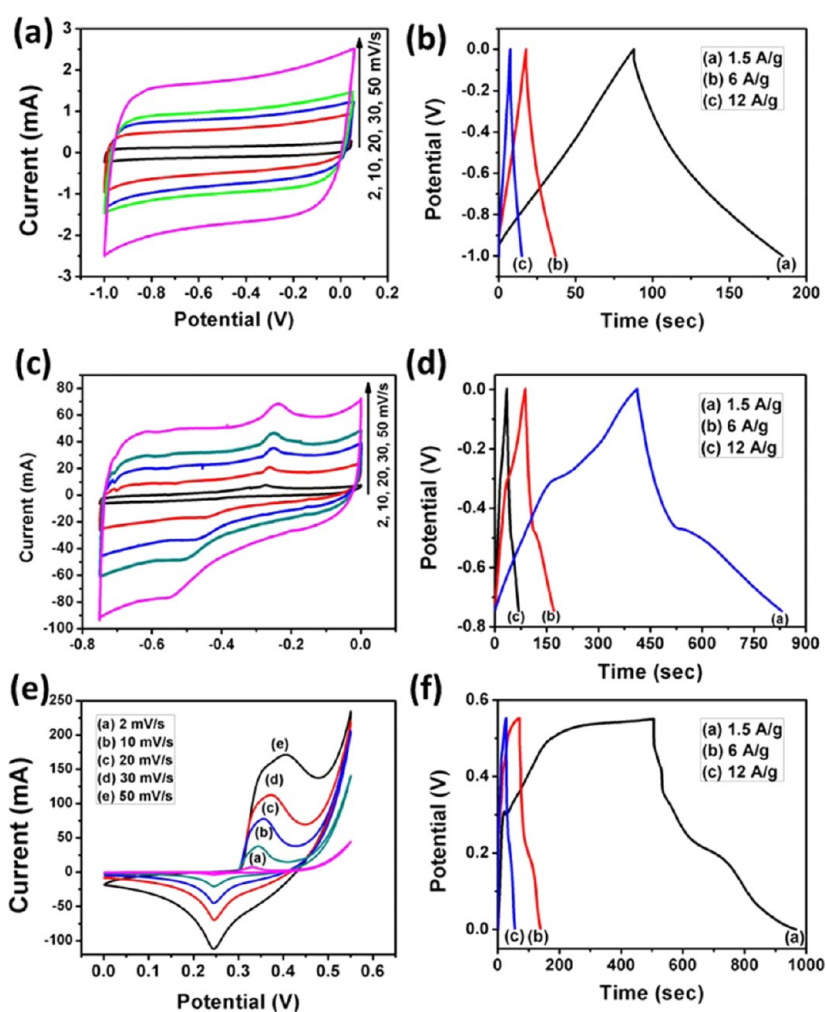

Figure 6. CV plots of (a) Ni@rGO, (c) Ni@Ni_3S_2, and (e) Ni@Co_3S_4 at different scan rates. GCD plots of (b) Ni@rGO, (d) Ni@Ni_3S_2, and (f) Ni@Co_3S_4 at different currents.
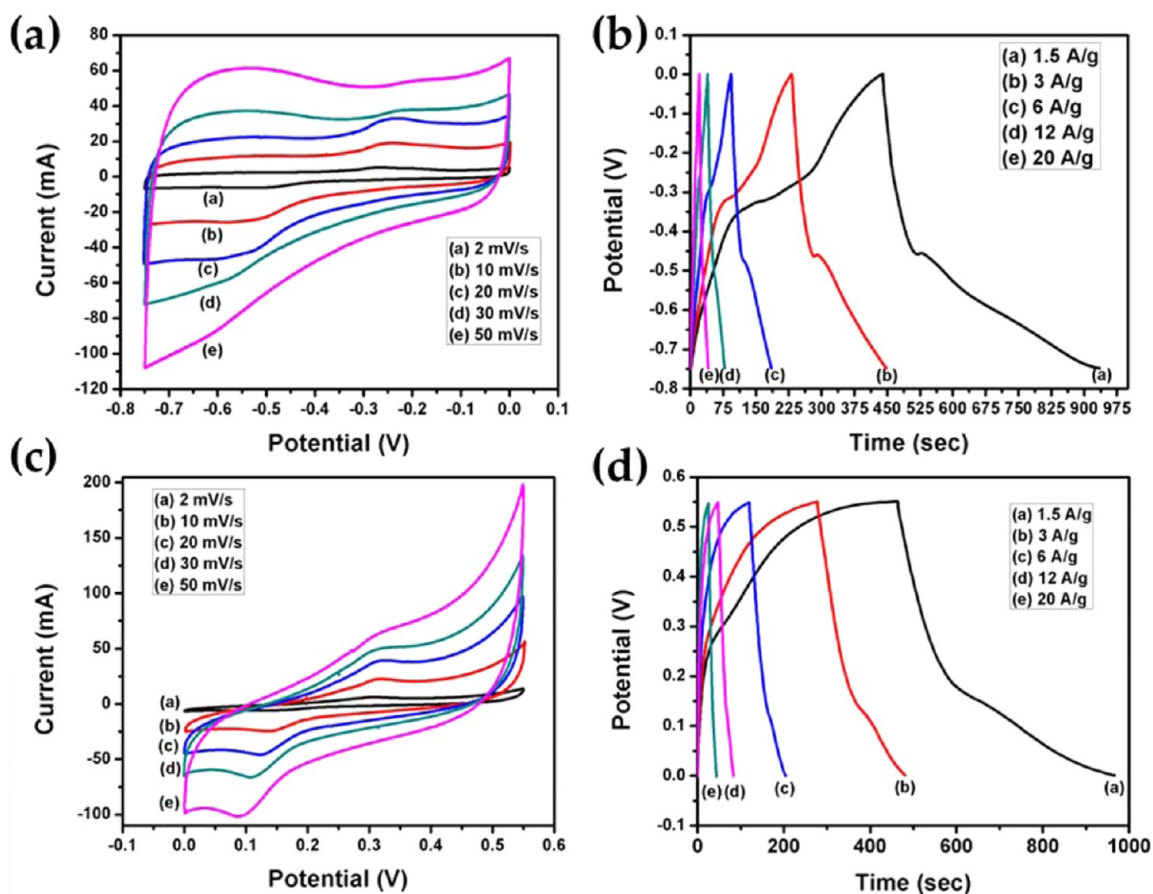
**Figure 7.** (a) CV and (b) GCD plots of Ni@rGO−Ni$_3$S$_2$. (c) CV and (d) GCD plots of Ni@rGO−Co$_3$S$_4$.

Co$_3$S$_4$ nanosheets are anchored on the rGO hydrogel. Both the Ni$_3$S$_2$ nanorods and Co$_3$S$_4$ cross-linked nanosheets are firmly attached to the rGO hydrogel. Even long-time sonication for the TEM sample preparation did not result in the separation of rGO from both Ni$_3$S$_2$ and Co$_3$S$_4$, indicating strong interaction of the metal sulfides with the rGO hydrogel.

The schematic diagram of the growth of a Ni$_3$S$_2$ nanorod and a Co$_3$S$_4$ nanosheet network over Ni@rGO is shown in Figure 5. Soaking of Ni@rGO in a Na$_2$S solution results in adsorption of the active S^{2-} ion on the rGO surface. The addition of Co^{2+} and Ni^{2+} ions results in the precipitation of corresponding metal sulfide nanoparticles on the rGO surface. Once the nucleation center is created, it triggers further growth of Ni$_3$S$_2$ and Co$_3$S$_4$ nanoparticles in the same direction. Hydrothermal treatment for a long time results in the orientation growth of the Ni$_3$S$_2$ nanorods with quite uniform size and shape, and 1D nanorod morphology is obtained following the Ostwald ripening mechanism. Although the initial growth of Co$_3$S$_4$ over rGO is likely to occur following the same growth mechanism of Ni$_3$S$_2$, the hydrothermal treatment of Co$_3$S$_4$ at high temperature for a long time results in their reorganization (possibly due to different interactions of the metal ions) and a cross-linked nanosheet network structure is obtained by the Ostwald ripening mechanism.

2.3. Electrochemical Characterizations. The Ni@rGO electrode was electrochemically characterized in terms of both cyclic voltammetry (CV) and galvanostatic charge−discharge (GCD) analysis within the potential range of −1 to −0 V, and the corresponding CV plots at different scan rates and GCD plots at different currents are shown in parts a and b of Figure

6, respectively. The rectangular nature of the CV plots confirms the formation of an efficient EDLC and fast charge propagation within the Ni@rGO electrode.[28] The maximum specific capacitance of 156 F/g was achieved for the Ni@rGO electrode at a 2 mV/s scan rate. The GCD plots of Ni@rGO show typical triangular behavior at each current of 1.5, 6, and 12 A/g, revealing the absence of pseudocapacitance distortion behavior and indicating typical double-layer capacitance behavior.

The maximum specific capacitance of 144 F/g was obtained from the GCD plot at 1.5 A/g current. CV analyses of Ni@Ni$_3$S$_2$ and Ni@Co$_3$S$_4$ were carried out within the potential ranges of −0.75 to 0 and 0−0.55 V, respectively, at various scan rates of 2, 10, 20, 30, and 50 mV/s, and the respective CV plots are shown in Figure 6c,e. Both electrodes exhibit a pair of redox peaks in the CV plots, indicating their typical pseudocapacitive behavior in the KOH electrolyte. In the case of Ni@Co$_3$S$_4$, the pseudocapacitance comes from the quasi-reversible electron-transfer process between the Co^{2+}/Co^{3+} redox couple in the presence of OH$^-$ ions.[29] The redox peaks in the CV plots of Ni@Ni$_3$S$_2$ also come from the redox reaction between the Ni^{2+}/Ni^{3+} redox couple in the presence of OH$^-$ following the equation[30]

$$Ni_3S_2 + 3OH^- \leftrightarrow Ni_3S_2(OH)_3 + 3e^-$$
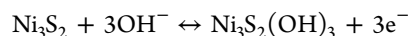
The maximum specific capacitances obtained from Ni@Ni$_3$S$_2$ and Ni@Co$_3$S$_4$ were 1019 and 1369 F/g, respectively, at 2 mV/s scan rate. Increasing scan rate resulted in decreasing specific capacitance, and the specific capacitances of 672 and 763 F/g were recorded at a high scan rate of 50 mV/s for the Ni@Ni$_3$S$_2$

and Ni@Co$_3$S$_4$ electrodes, respectively. The GCD plots of Ni@Ni$_3$S$_2$ and Ni@Co$_3$S$_4$ at different currents of 1.5, 6, and 12 A/g are shown in parts d and f of Figure 6, respectively. All of the GCD plots show typical nonlinear behavior, also confirming their pseudocapacitive nature. The maximum specific capacitances of 834 and 1260 F/g were obtained for the Ni@Ni$_3$S$_2$ and Ni@Co$_3$S$_4$ electrodes, respectively, at 1.5 A/g current.

The electrochemical characterizations of Ni@rGO−Ni$_3$S$_2$ and Ni@rGO−Co$_3$S$_4$ were carried out within the same potential region as that used for Ni@Ni$_3$S$_2$ and Ni@Co$_3$S$_4$, respectively, and their respective CV plots at various scan rates of 2, 10, 20, 30, and 50 mV/s are shown in Figure 7a,c. The CV plots of both Ni@rGO−Ni$_3$S$_2$ and Ni@rGO−Co$_3$S$_4$ also show a pair of redox peaks, indicating typical pseudocapacitive behavior in a 6 M KOH electrolyte. With increasing scan rate, the total current increases in the CV plots, clearly indicating a diffusion-controlled phenomenon, which is a slow process. Depending on the voltage scan rate, the diffusion layer size above the electrode surface is changed. A higher scan rate results in a decreased difference between the diffusion layer and electrode surface, which indeed results in increased flux to the electrode surface; hence, a higher current is achieved. The redox peaks showed a little shifting, which resulted in increased peak separation with increasing scan rate. The peak separation is due to solution resistance and a major effect of the iR drop. The increasing peak separation with increasing scan rate also indicates a quasi-reversible process, where the heterogeneous electron-transfer rate is slow compared to the time scale of the experiment.[31] The maximum specific capacitances calculated from the CV plots were 1165.8 and 1463.4 F/g, respectively, for the Ni@rGO−Ni$_3$S$_2$ and Ni@rGO−Co$_3$S$_4$ electrodes at 2 mV/s scan rate.

The various specific capacitances obtained from all of the Ni@rGO, Ni@Ni$_3$S$_2$, Ni@Co$_3$S$_4$, Ni@rGO−Ni$_3$S$_2$, and Ni@rGO−Co$_3$S$_4$ electrodes at different scan rates are shown in Table 1.

Table 1. Scan-Rate-Dependent Specific Capacitances (F/g) of the Ni@rGO, Ni@Ni$_3$S$_2$, Ni@Co$_3$S$_4$, Ni@rGO−Ni$_3$S$_2$, and Ni@rGO−Co$_3$S$_4$ Electrodes

	scan rate (mV/s)				
	2	10	20	30	50
specific capacitance of Ni@rGO	156	129	111	101	84
specific capacitance of Ni@Ni$_3$S$_2$	1019	842	798	729	672
specific capacitance of Ni@Co$_3$S$_4$	1369	1031	928	847	763
specific capacitance of Ni@rGO−Ni$_3$S$_2$	1165.8	976.6	890.3	822.7	752
specific capacitance of Ni@rGO−Co$_3$S$_4$	1463.4	1112.4	1002	922	821

The specific capacitances obtained at different scan rates for both Ni@rGO−Ni$_3$S$_2$ and Ni@rGO−Co$_3$S$_4$ were considerably higher than the virgin Ni@Ni$_3$S$_2$ and Ni@Co$_3$S$_4$, respectively. This clearly signifies that the rGO hydrogel does not just act as a basal plane for the growth of Ni$_3$S$_2$ nanorods and Co$_3$S$_4$ cross-linked nanosheet networks, but rather some sort of synergistic interaction is there between the rGO and metal sulfide to lift the specific capacitance to a higher value. The interaction of metal sulfides with rGO hydrogels occurs probably via a linkage of thiol bonds between the metal sulfide and residual surface

group of the rGO hydrogel.[32] The increasing scan rate resulted in a decreased specific capacitance. However, both the Ni@rGO−Ni$_3$S$_2$ and Ni@rGO−Co$_3$S$_4$ electrode materials showed excellent rate capability, as is obvious from their respective specific capacitance retentions of 64.5% and 56.1% at a high scan rate of 50 mV/s with respect to the low scan rate of 2 mV/s. The CV plot of the Ni@rGO−Ni$_3$S$_2$ electrode exhibits more symmetrical behavior than that of Ni@rGO−Co$_3$S$_2$, with a quite rectangular-shaped CV plot also indicating its better reversibility.

The GCD plots of the Ni@rGO−Ni$_3$S$_2$ and Ni@rGO−Co$_3$S$_4$ electrodes at different mass normalized currents of 1.5, 3, 6, 12, and 20 A/g are shown in parts b and d of Figure 7, respectively. Both materials showed a slight nonlinear charge−discharge plot, which also supports their deviation from ideal character, where the specific capacitance is mainly contributed by the redox reaction. The maximum specific capacitances obtained from the Ni@rGO−Ni$_3$S$_2$ and Ni@rGO−Co$_3$S$_4$ electrodes were 987.8 and 1369 F/g, respectively, at a low mass normalized current of 1.5 A/g. The specific capacitance exhibited a linear decrease with increasing current due to the quick attainment of the operating voltage range at high current, resulting in a fast charge−discharge. Still, the high current responses of both electrodes were outstanding with high specific capacitances of 536.7 and 684.5 F/g, respectively, for Ni@rGO−Ni$_3$S$_2$ and Ni@rGO−Ni$_3$S$_2$ at 20 A/g. The high rate capability of both electrodes must correspond to the very low electron spin resonance (ESR) of the electrode materials, as is obvious from the least iR drop at the discharge plot even at high mass normalized current.

Although both electrodes showed high specific capacitance and excellent rate capability, the low working potential restricts their energy and power densities. The maximum energy densities of 77.17 and 57.51 Wh/kg were obtained for Ni@rGO−Ni$_3$S$_2$ and Ni@rGO−Ni$_3$S$_2$ at the respective power densities of 562.5 and 412.5 W/kg. For the symmetric supercapacitors consisting of two identical rGO@Ni−Ni$_3$S$_2$ and rGO@Ni−Co$_3$S$_4$ electrodes, the specific capacitance would be one-fourth that of a single electrode tested in a three-electrode configuration.[33,34] Considering the specific capacitance of the rGO@Ni−Ni$_3$S$_2$ and rGO@Ni−Co$_3$S$_4$ electrodes from GCD analysis within the potential ranges of −0.75 to 0 and 0−0.55 V, respectively, the maximum energy densities of 19.29 and 14.38 Wh/kg can be obtained. However, the low cell voltage restricts their energy density. To address the issue, an asymmetric supercapacitor was fabricated using Ni@rGO−Ni$_3$S$_2$ as the negative electrode and Ni@rGO−Co$_3$S$_4$ as the positive electrode. The Ni@rGO−Co$_3$S$_4$//Ni@rGO−Ni$_3$S$_2$ electrode showed a large cell voltage of 1.3 V. The stable working potential was chosen by considering the Coulombic efficiency from the GCD test at low mass normalized current. Beyond the potential range, the Coulombic efficiency was too high to compensate for the energy density. The CV plots of the Ni@rGO−Co$_3$S$_4$//Ni@rGO−Ni$_3$S$_2$ asymmetric supercapacitor at different scan rates are shown in Figure 8a. The CV plots also exhibit two pairs of redox peaks during the positive and negative sweeps, indicating typical pseudocapacitive behavior coming from both Co$_3$S$_4$ and Ni$_3$S$_2$. The maximum specific capacitance obtained from the CV plot of the asymmetric supercapacitor was 1044 F/g at 2 mV/s scan rate. To further evaluate the practical application of the Ni@rGO−Co$_3$S$_4$//Ni@rGO−Ni$_3$S$_2$ electrode, the GCD test was carried out at different mass normalized currents of 1.5, 3, 6, 12,
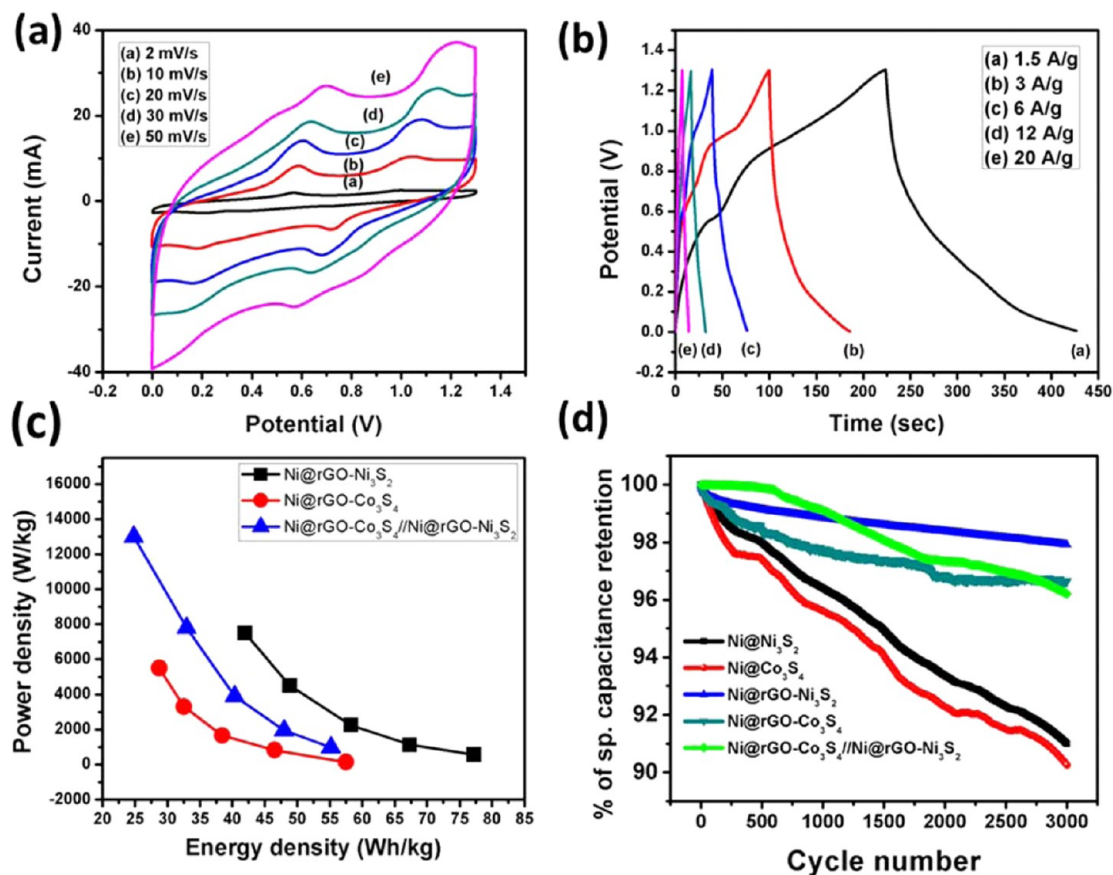
Figure 8. (a) CV plots at different scan rates and (b) GCD plots at different currents of Ni@rGO−Co$_3$S$_4$//Ni@rGO−Ni$_3$S$_2$. (c) Variation of the energy density with the power density. (d) Percentage of specific capacitance retention with the cycle number of Ni@Ni$_3$S$_2$, Ni@Co$_3$S$_4$, Ni@rGO−Ni$_3$S$_2$, Ni@rGO−Co$_3$S$_4$, and Ni@rGO−Co$_3$S$_4$//Ni@rGO−Ni$_3$S$_2$.

and 20 A/g, and the plots are shown in Figure 8b. The maximum specific capacitance obtained was 940 F/g at 1.5 A/g. The various specific capacitances obtained at different mass normalized currents are shown in Table 2.

Table 2. Mass-Normalized-Current-Dependent Specific Capacitances (F/g) of Ni@rGO−Ni$_3$S$_2$, Ni@rGO−Co$_3$S$_4$, and Ni@rGO−Co$_3$S$_4$//Ni@rGO−Ni$_3$S$_2$

	mass normalized current (A/g)				
	1.5	3	6	12	20
specific capacitance of Ni@rGO−Ni$_3$S$_2$	987.8	861.8	745.9	625	536.8
specific capacitance of Ni@rGO−Co$_3$S$_4$	1369	1107.3	926.4	774.5	684.5
specific capacitance of Ni@rGO−Co$_3$S$_4$//Ni@rGO−Ni$_3$S$_2$	940	817.2	688	561.2	432.2

The maximum energy density calculated from Ni@rGO−Co$_3$S$_4$//Ni@rGO−Ni$_3$S$_2$ was 55.16 Wh/kg at a high power delivery rate of 975 W/kg. The increased power density did not result in a significant loss of energy density, and a high energy density of 24.84 Wh/kg was achieved at a very high power delivery rate of 13000 W/kg. The maximum specific energy density is much higher or somewhere comparable than some other reported related asymmetric supercapacitors, such as

AC//Co(OH)$_2$ (25.7 Wh/kg),[35] CNT/Ni(OH)$_2$//AC (16.8 Wh/kg at 400 W/kg),[36] AC//NiO (15−20 Wh/kg),[37] CNTs/MnO$_2$//CNTs/SnO$_2$ (20.3 Wh/kg),[38] Ni(OH)$_2$//graphene (30 Wh/kg).[39] Ni(OH)$_2$/CNT-AC (32.5 Wh/kg at a power density of 1800 W/kg),[40] AC//Ni$_3$S$_2$/CNT (19.8 Wh/kg),[41] nickel−cobalt sulfide//AC (25 Wh/kg),[42] NiCo$_2$S$_4$//RGO (31.5 Wh/kg),[43] and CoS$_2$//AC (37 Wh/kg).[44] Variation of the energy density with the power density of Ni@rGO−Ni$_3$S$_2$, Ni@rGO−Co$_3$S$_4$, and Ni@rGO−Co$_3$S$_4$//Ni@rGO−Ni$_3$S$_2$ is shown in Figure 6c. In order to understand the cycle life of the as-fabricated electrodes, the GCD tests were continued to 3000 consecutive charge−discharge cycles at 12 A/g for all of the Ni@Ni$_3$S$_2$, Ni@Co$_3$S$_4$, Ni@rGO−Ni$_3$S$_2$, Ni@rGO−Co$_3$S$_4$, and Ni@rGO−Co$_3$S$_4$//Ni@rGO−Ni$_3$S$_2$ electrodes, and the respective specific capacitance retentions of 91%, 90.3%, 97.9%, 96.6%, and 96.2% were achieved at the end. The plot of the percentage of specific capacitance retention with the cycle number is shown in Figure 8d. The very high specific capacitance retention of Ni@rGO−Ni$_3$S$_2$ and Ni@rGO−Co$_3$S$_4$ over Ni@Ni$_3$S$_2$ and Ni@Co$_3$S$_4$ can be attributed to the presence of a flexible rGO hydrogel sandwiched between Ni$_3$S$_2$ and Ni foam and between Co$_3$S$_4$ and Ni foam. The high flexibility of rGO releases the mechanical strain faced by the pseudocapacitive metal sulfides during the consecutive charge−discharge cycles. Besides, it also strongly binds the metal sulfides possibly through both chemical covalent bonding at the sulfur-containing sites and van der Waals interaction with conjugated domains of graphene. Thus, both Ni$_3$S$_2$ and Co$_3$S$_4$

are strongly anchored on Ni@rGO, which minimizes the possibility of degradation of the electrode material.

The electrochemical impedance spectroscopy of the as-prepared Ni@rGO−Ni$_3$S$_2$, Ni@rGO−Co$_3$S$_4$, and Ni@rGO−Co$_3$S$_4$//Ni@rGO−Ni$_3$S$_2$ electrodes were carried out within the frequency range of 100 kHz to 0.01 Hz and have been represented in terms of the Nyquist plot in Figure 9a. All three
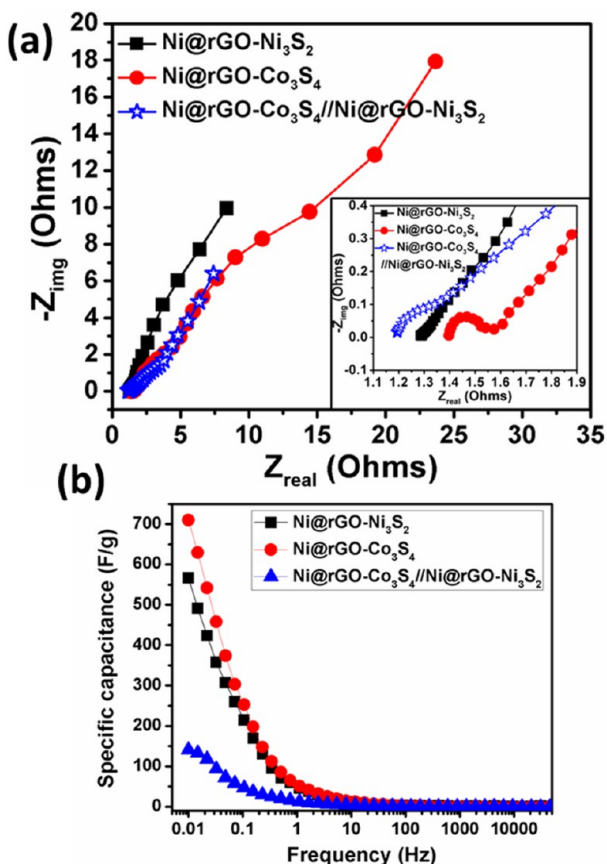

Figure 9. (a) Nyquist plots of Ni@rGO−Ni$_3$S$_2$, Ni@rGO−Co$_3$S$_4$, and Ni@rGO−Co$_3$S$_4$//Ni@rGO−Ni$_3$S$_2$ and (b) their variation of the specific capacitance with frequency.

electrodes showed low ESR at 1.29, 1.19, and 1.4 Ω, respectively. Variation of the specific capacitances of the Ni@rGO−Ni$_3$S$_2$, Ni@rGO−Co$_3$S$_4$, and Ni@rGO−Co$_3$S$_4$//Ni@rGO−Ni$_3$S$_2$ electrodes as a function of the frequency is shown in Figure 9b. With increasing frequency, the specific capacitances showed a rapid decrease, and at high frequency, all three electrodes exhibited very low specific capacitance. Thus, the electrodes showed capacitor behavior at the low-frequency region and resistor behavior at the high-frequency region.

3. CONCLUSION

Ni foam@rGO hydrogel−Ni$_3$S$_2$ and Ni foam@rGO hydrogel−Co$_3$S$_4$ composites were successfully synthesized by a two-step hydrothermal approach, where the rGO hydrogel was sandwiched between the metal sulfide and Ni foam substrate. Sonochemical deposition of the flame-induced rGO paper on Ni foam followed by hydrothermal treatment resulted in the formation of rGO-hydrogel-coated Ni foam. A hydrothermal treatment of the Ni@rGO foam substrate with the corresponding metal nitrate and sodium sulfide resulted in the formation of porous Ni$_3$S$_2$ nanorods and Co$_3$S$_4$ self-assembled nanopetals

uniformly grown over the Ni@rGO substrate. Both Ni@rGO−Ni$_3$S$_2$ and Ni@rGO−Co$_3$S$_4$ were electrochemically characterized in a 6 M KOH electrolyte, which showed high specific capacitances of 987.8 and 1369 F/g, respectively, at 1.5 A/g mass normalized current accompanied by very high cycle stability. An advanced aqueous asymmetric (AAS) supercapacitor was fabricated by exploiting Ni@rGO−Co$_3$S$_4$ as a positive electrode and Ni@rGO−Ni$_3$S$_2$ as a negative electrode. The as-fabricated AAS exhibited a very high energy density of 55.16 Wh/kg at a high power density of 975 W/kg and a high energy density of 24.84 Wh/kg at a very high power delivery rate of 13000 W/kg accompanied by high cycle stability, which makes it an efficient candidate in the field of supercapacitor.

4. EXPERIMENTAL SECTION

4.1. Synthesis of GO and rGO Papers. GO was synthesized using a modified Hummers method and described elsewhere.[45] The GO paper was prepared from a GO aqueous colloid.[46] In brief, 100 mg of solid GO was dispersed in 200 mL of H$_2$O by ultrasonication for 1 h at high power, followed by centrifugation for 15 min at 3000 rpm, forming a black-brown GO aqueous colloid. A total of 20 mL of the GO aqueous colloid was diluted with 20 mL of H$_2$O and filtered through a filter paper of 0.45 μm pore size, followed by washing, air drying, and detachment from the filter paper to obtain the GO paper. The GO paper was reduced by a butane flame to prepare the rGO paper.

4.2. Preparation of Composite Materials. Part (20 mg) of the as-prepared rGO paper was dispersed in 30 mL of H$_2$O by ultrasonication for 1 h, keeping two pieces of cleaned Ni foam (1 × 1 cm^2) inside the solution vertically aligned. The ultrasonication process helps the dispersed rGO to deposit on the Ni foam. A post hydrothermal treatment of the whole suspension along with the Ni foam in a 50 mL capacity Teflon-sealed autoclave at 180 °C for 6 h resulted in formation of the rGO hydrogel on the Ni foam (Ni@rGO). Then the two Ni@rGO were dried at 70 °C. The mass of deposited rGO on the Ni foam substrate was about ∼0.88 mg. The two as-prepared Ni@rGO were then soaked individually in 10 mL of a 0.1 M Na$_2$S solution for 10 min in two 50 mL capacity Teflon-sealed autoclaves, and 10 mL of 0.1 M Ni(NO$_3$)$_2$ and 10 mL of 0.1 M Co(NO$_3$)$_2$ were poured in each autoclave at once with gentle shaking. An immediate precipitation occurred. Then the two autoclaves were maintained at 120 °C for 6 h. The hydrothermal treatment helps to grow the corresponding metal sulfide directly on Ni foam, and almost pure phase on Ni$_3$S$_2$ and Co$_3$S$_4$ on Ni@rGO were obtained. The Ni foam substrate containing all of the materials was washed with a stream of distilled water in order to remove the extra precipitation from Ni@rGO, which had no direct contact with the substrate. The as-prepared materials were labeled as Ni@rGO−Ni$_3$S$_2$ and Ni@rGO−Co$_3$S$_4$, respectively, with respective masses of 2.8 and 2.7 mg of the active material. Ni$_3$S$_2$ and Co$_3$S$_4$ were also grown directly on the cleaned Ni foam substrate without using rGO, using the same amount of precursor at the same reaction conditions.

4.3. Preparation of Electrodes. The Ni@rGO, Ni@Ni$_3$S$_2$, Ni@Co$_3$S$_4$, Ni@rGO−Ni$_3$S$_2$, and Ni@rGO−Co$_3$S$_4$ electrodes were electrochemically characterized in a three-electrode cell, where platinum and saturated calomel electrodes were used as the counter and reference electrodes, respectively, in a 6 M KOH aqueous electrolyte. An asymmetric supercapacitor was fabricated using the as-prepared Ni@rGO−Ni$_3$S$_2$ as the negative electrode and Ni@rGO−Co$_3$S$_4$ as the positive electrode, directly separated by a distance of 2 cm with Whatman filter paper as the separator in a 6 M KOH electrolyte. Platinum wire was used for the current connection between the electrode and instrument. The performance of an asymmetric supercapacitor depends on the charge balance in both electrodes, i.e., $q^+(m^+C^+V^+) = q^-(m^-C^-V^-)$.[47]

Following this equation, considering the specific capacitance at 1.5 A/g, the optimum mass ratio of anode to cathode is 0.98, which is very close to the used active material mass ratio of 0.96.

■ ASSOCIATED CONTENT

Ⓢ Supporting Information

Materials used, characterization techniques and instruments, equations used for measurement of the electrochemical result, pore size distribution of the rGO hydrogel, FESEM images of Ni@Ni$_3$S$_2$ and Ni@Co$_3$S$_4$, elemental analyses of Ni@rGO−Ni$_3$S$_2$ and Ni@rGO−Co$_3$S$_4$, and FESEM images and CV plots of Ni@rGO−Ni$_3$S$_2$ and Ni@rGO−Co$_3$S$_4$ after 15 h of hydrothermal treatment. This material is available free of charge via the Internet at http://pubs.acs.org.

■ AUTHOR INFORMATION

Corresponding Author

*E-mail: chapal12@yahoo.co.in.

Notes

The authors declare no competing financial interest.

■ ACKNOWLEDGMENTS

■ REFERENCES

(1) Conway, B. *Electrochemical Supercapacitors*, 2nd ed.; Kluwer Academic/Plenum Publishers: New York, 1999.

(2) Ghosh, D.; Giri, S.; Das, C. K. Hydrothermal Synthesis of Platelet β Co(OH)$_2$ and Co$_3$O$_4$: Smart Electrode Material for Energy Storage Application. *Environ. Prog. Sustainable Energy* **2014**, 33, 1059−1064.

(3) Yuan, C.; Zhang, X.; Su, L.; Gao, B.; Shen, L. Facile Synthesis and Self-Assembly of Hierarchical Porous NiO Nano/Micro Spherical Superstructures for High Performance Supercapacitors. *J. Mater. Chem.* **2009**, 19, 5772−5777.

(4) Ghosh, D.; Giri, S.; Das, C. K. Preparation of CTAB-Assisted Hexagonal Platelet Co(OH)$_2$/Graphene Hybrid Composite as Efficient Supercapacitor Electrode Material. *ACS Sustainable Chem. Eng.* **2013**, 1, 1135−1142.

(5) Ghosh, D.; Giri, S.; Mandal, A.; Das, C. K. Graphene Decorated with Ni(OH)$_2$ and Ag Deposited Ni(OH)$_2$ Stacked Nanoplate for Supercapacitor Application. *Chem. Phys. Lett.* **2013**, 573, 41−47.

(6) Yu, X.; Lu, B.; Xu, Z. Super Long-Life Supercapacitors Based on the Construction of Nanohoneycomb-Like Strongly Coupled CoMoO$_4$−3D Graphene Hybrid Electrodes. *Adv. Mater.* **2014**, 26, 1044−1051.

(7) Ghosh, D.; Giri, S.; Das, C. K. Synthesis, Characterization and Electrochemical Performance of Graphene Decorated with 1D NiMoO$_4$·nH$_2$O Nanorods. *Nanoscale* **2013**, 5, 10428−10437.

(8) Rui, X.; Tan, H.; Yan, Q. Nanostructured Metal Sulfides for Energy Storage. *Nanoscale* **2014**, 6, 9889−9924.

(9) Zhu, T.; Wang, Z.; Ding, S.; Chen, J. S.; Lou, X. W. Hierarchical Nickel Sulfide Hollow Spheres for High Performance Supercapacitors. *RSC Adv.* **2011**, 1, 397−400.

(10) Yang, J.; Duan, X.; Qin, Q.; Zheng, W. Solvothermal Synthesis of Hierarchical Flower-like β-NiS with Excellent Electrochemical Performance for Supercapacitors. *J. Mater. Chem. A* **2013**, 1, 7880−7884.

(11) Pang, H.; Wei, C.; Li, X.; Li, G.; Ma, Y.; Li, S.; Chen, J.; Zhang, J. Microwave-Assisted Synthesis of NiS$_2$ Nanostructures for Supercapacitors and Cocatalytic Enhancing Photocatalytic H$_2$ Production. *Sci. Rep.* **2014**, 4, 1−8.

(12) Krishnamoorthya, K.; Veerasubramanib, G. K.; Radhakrishnana, S.; Kim, S. J. One Pot Hydrothermal Growth of Hierarchical Nanostructured Ni$_3$S$_2$ on Ni Foam for Supercapacitor Application. *Chem. Eng. J.* **2014**, 251, 116−122.

(13) Xing, J. C.; Zhou, Q. W.; Zhu, Y. L.; Jiao, Q. J.; Zheng, X. D. Fabrication and Shape Evolution of CoS$_2$ Octahedrons for Application in Supercapacitors. *Electrochim. Acta* **2014**, 136, 550−556.

(14) Bao, S. J.; Li, C. M.; Guo, C. X.; Qiao, Y. Biomolecule-Assisted Synthesis of Cobalt Sulfide Nanowires for Application in Supercapacitors. *J. Power Sources* **2008**, 180, 676−681.

(15) Yang, Z.; Chen, C. Y.; Chang, H. T. Supercapacitors Incorporating Hollow Cobalt Sulfide Hexagonal Nanosheets. *J. Power Sources* **2011**, 196, 7874−7877.

(16) Wan, H.; Ji, X.; Jiang, J.; Yu, J.; Miao, L.; Zhang, L.; Bie, S.; Chen, H.; Ruan, Y. Hydrothermal Synthesis of Cobalt Sulfide Nanotubes: The Size Control and Its Application in Supercapacitors. *J. Power Sources* **2013**, 243, 396−402.

(17) Justin, P.; Rao, G. R. CoS Spheres for High-Rate Electrochemical Capacitive Energy Storage Application. *Int. J. Hydrogen Energy* **2010**, 35, 9709−9715.

(18) Luo, F.; Li, J.; Yuan, H.; Xiao, D. Rapid Synthesis of Three-Dimensional Flower-like Cobalt Sulfide Hierarchitectures by Microwave Assisted Heating Method for High-Performance Supercapacitors. *Electrochim. Acta* **2014**, 123, 183−189.

(19) Ramadoss, A.; Kim, T.; Kim, G.-S.; Kim, S. J. Enhanced Activity of a Hydrothermally Synthesized Mesoporous MoS$_2$ Nanostructure for High Performance Supercapacitor Applications. *New J. Chem.* **2014**, 38, 2379−2385.

(20) Wang, X.; Ding, J.; Yao, S.; Wu, X.; Feng, Q.; Wang, Z.; Geng, B. High Supercapacitor and Adsorption Behaviors of Flower-like MoS$_2$ Nanostructures. *J. Mater. Chem. A* **2014**, 2, 15958−15963.

(21) Ratha, S.; Rout, C. S. Supercapacitor Electrodes Based on Layered Tungsten Disulfide-Reduced Graphene Oxide Hybrids Synthesized by a Facile Hydrothermal Method. *ACS Appl. Mater. Interfaces* **2013**, 5, 11427−11433.

(22) Wang, Q.; Jiao, L.; Du, H.; Si, Y.; Wang, Y.; Yuan, H. Co$_3$S$_4$ Hollow Nanospheres Grown on Graphene as Advanced Electrode Materials for Supercapacitors. *J. Mater. Chem.* **2012**, 22, 21387−21391.

(23) Qu, B.; Chen, Y.; Zhang, M.; Hu, L.; Lei, D.; Lu, B.; Li, Q.; Wang, Y.; Chen, L.; Wang, T. β-Cobalt Sulfide Nanoparticles Decorated Graphene Composite Electrodes for High Capacity and Power Supercapacitors. *Nanoscale* **2012**, 4, 7810−7816.

(24) Wang, A.; Wang, H.; Zhang, S.; Mao, C.; Song, J.; Niu, H.; Jin, B.; Tian, Y. Controlled Synthesis of Nickel Sulfide/Graphene Oxide Nanocomposite for High-Performance Supercapacitor. *Appl. Surf. Sci.* **2013**, 282, 704−708.

(25) Zhang, H.; Yu, X.; Guo, D.; Qu, B.; Zhang, M.; Li, Q.; Wang, T. Synthesis of Bacteria Promoted Reduced Graphene Oxide−Nickel Sulfide Networks for Advanced Supercapacitors. *ACS Appl. Mater. Interfaces* **2013**, 5, 7335−7340.

(26) Dai, C. S.; Chien, P. Y.; Lin, J. Y.; Chou, S. W.; Wu, W. K.; Li, P. H.; Wu, K. Y.; Lin, T. W. Hierarchically Structured Ni$_3$S$_2$/Carbon Nanotube Composites as High Performance Cathode Materials for Asymmetric Supercapacitors. *ACS Appl. Mater. Interfaces* **2013**, 5, 12168−12174.

(27) Volfkovich, Y. M.; Mikhailin, A. A.; Bograchev, D. A.; Sosenkin, V. E.; Bagotsky, V. S. *Studies of Supercapacitor Carbon Electrodes with High Pseudocapacitance*; InTech: New York, 2012; Chapter 7, pp 159−182.

(28) El-Kady, M. F.; Kaner, R. B. Scalable Fabrication of High-Power Graphene Micro-Supercapacitors for Flexible and On-Chip Energy Storage. *Nat. Commun.* **2013**, 4, 1−9.

(29) Zhang, Q.; Xu, C.; Lu, B. Super-Long Life Supercapacitors Based on the Construction of Ni Foam/Graphene/Co$_3$S$_4$ Composite Film Hybrid Electrodes. *Electrochim. Acta* **2014**, 132, 180−185.

(30) Xing, Z.; Chu, Q.; Ren, X.; Gea, C.; Qusti, A. H.; Asiri, A. M.; Al-Youbi, A. O.; Sun, X. Ni$_3$S$_2$ Coated ZnO Array for High-Performance Supercapacitors. *J. Power Sources* **2014**, 245, 463−467.

(31) He, P.; Faulkner, L. R. Cybernetic Control of an Electrochemical Repertoire. *Anal. Chem.* **1982**, 54, 1313A−1326A.

(32) Geng, H.; Kong, S. F.; Wang, Y. NiS Nanorod-Assembled Nanoflowers Grown on Graphene: Morphology Evolution and Li-ion Storage Applications. *J. Mater. Chem. A* **2014**, 2, 15152−15158.

(33) Nam, K. W.; Lee, C. W.; Yang, X. Q.; Cho, B. W.; Yoon, W. S.; Kim, K. B. Electrodeposited Manganese Oxides on Three-Dimensional

Carbon Nanotube Substrate: Supercapacitive Behaviour in Aqueous and Organic Electrolytes. *J. Power Sources* **2009**, *188*, 323−331.

(34) Yan, J.; Liu, J.; Fan, Z.; Wei, T.; Zhang, L. High-Performance Supercapacitor Electrodes Based on Highly Corrugated Graphene Sheets. *Carbon* **2012**, *50*, 2179−2188.

(35) Kong, L. B.; Liu, M.; Lang, J. W.; Luo, Y. C.; Kang, L. Asymmetric Supercapacitor Based on Loose-Packed Cobalt Hydroxide Nanoflake Materials and Activated Carbon. *J. Electrochem. Soc.* **2009**, *156*, A1000−A1004.

(36) Wang, X.-f.; Ruan, D.-b.; You, Z. Application of Spherical $Ni(OH)_2$/CNTs Composite Electrode in Asymmetric Supercapacitor. *Trans. Nonferrous Met. Soc. China* **2006**, *16*, 1129−1134.

(37) Wang, D. W.; Li, F.; Cheng, H. M. Hierarchical Porous Nickel Oxide and Carbon as Electrode Materials for Asymmetric Super-capacitor. *J. Power Sources* **2008**, *185*, 1563−1568.

(38) Ng, K. C.; Zhang, S.; Chen, G. Z. An Asymmetrical Supercapacitor Based on CNTs/SnO_2 and CNTs/MnO_2 Nano-composites Working at 1.7 V in Aqueous Electrolyte. *ECS Trans.* **2008**, *16*, 153−162.

(39) Lang, J.-W.; Kong, L.-B.; Liu, M.; Luo, Y.-C.; Kang, L. Asymmetric Supercapacitors Based on Stabilized α-$Ni(OH)_2$ and Activated Carbon. *J. Solid State Electrochem.* **2010**, *14*, 1533−1539.

(40) Li, H. B.; Yu, M. H.; Wang, F. X.; Liu, P.; Liang, Y.; Xiao, J.; Wang, C. X.; Tong, Y. X.; Yang, G. W. Amorphous Nickel Hydroxide Nanospheres with Ultrahigh Capacitance and Energy Density as Electrochemical Pseudocapacitor Materials. *Nat. Commun.* **2013**, *4*, 1−7.

(41) Dai, C. S.; Chien, P. Y.; Lin, J. Y.; Chou, S. W.; Wu, W. K.; Li, P. H.; Wu, K. Y.; Lin, T. W. Hierarchically Structured Ni_3S_2/Carbon Nanotube Composites as High Performance Cathode Materials for Asymmetric Supercapacitors. *ACS Appl. Mater. Interfaces* **2013**, *5*, 12168−12174.

(42) Li, Y.; Cao, L.; Qiao, L.; Zhou, M.; Yang, Y.; Xiao, P.; Zhang, Y. Ni−Co sulfide nanowires on nickel foam with ultrahigh capacitance for asymmetric supercapacitors. *J. Mater. Chem. A* **2014**, *2*, 6540−6548.

(43) Chen, H.; Jiang, J.; Zhang, L.; Xia, D.; Zhao, Y.; Guo, D.; Qi, T.; Wan, H. In situ Growth of $NiCo_2S_4$ Nanotube Arrays on Ni Foam for Supercapacitors: Maximizing Utilization Efficiency at High Mass Loading to Achieve Ultrahigh Areal Pseudocapacitance. *J. Power Sources* **2014**, *254*, 249−257.

(44) Amaresh, S.; Karthikeyan, K.; Jang, I.-C.; Lee, Y. S. Single-Step Microwave Mediated Synthesis of the CoS_2 Anode Material for High Rate Hybrid Supercapacitors. *J. Mater. Chem. A* **2014**, *2*, 11099−11106.

(45) Xu, Y. X.; Bai, H.; Lu, G. W.; Li, C.; Shi, G. Q. Flexible Graphene Films via the Filtration of Water-Soluble Noncovalent Functionalized Graphene Sheets. *J. Am. Chem. Soc.* **2008**, *130*, 5856−5857.

(46) Sun, D.; Yan, X.; Lang, J.; Xue, Q. High Performance Supercapacitor Electrode Based on Graphene Paper via Flame-Induced Reduction of Graphene Oxide Paper. *J. Power Sources* **2013**, *222*, 52−58.

(47) Huo, H.; Zhao, Y.; Xu, C. 3D Ni_3S_2 Nanosheet Arrays Supported on Ni Foam for High-Performance Supercapacitor and Non-Enzymatic Glucose Detection. *J. Mater. Chem. A* **2014**, *2*, 15111−15117.